Monthly Notices of the ROYAL ASTRONOMICAL SOCIETY

MNRAS **519,** 2940–2950 (2023) https://doi.org/10.1093/mnras/stac3609
Advance Access publication 2022 December 12

Quantifying the dust in SN 2012aw and iPTF14hls with ORBYTS

Maria Niculescu-Duvaz,[1] M. J. Barlow,[1]★ William Dunn,[1] Antonia Bevan,[1] Omar Ahmed,[2] David Arkless,[2] Jon Barker,[2] Sidney Bartolotta,[2] Liam Brockway,[2] Daniel Browne,[2] Ubaid Esmail,[2] Max Garner,[2] Wiktoria Guz,[2] Scarlett King,[2] Hayri Kose,[2] Madeline Lampstaes-Capes,[2] Joseph Magen,[2] Nicole Morrison,[2] Kyaw Oo,[2] Balvinder Paik,[2] Joanne Primrose,[2] Danny Quick,[2] Anais Radeka,[2] Anthony Rodney,[2] Eleanor Sandeman,[2] Fawad Sheikh,[2] Camron Stansfield,[2] Delayne Symister,[2] Joshua Taylor,[2] William Wilshere,[2] R. Wesson,[1] I. De Looze,[3] G. C. Clayton,[4] K. Krafton[4] and M. Matsuura[5]

[1]*Department of Physics & Astronomy, University College London, Gower St, London WC1E 6BT, UK*
[2]*Highams Park School, Handsworth Avenue, Highams Park, London E4 9PJ, UK*
[3]*Sterrenkundig Observatorium, Ghent University, Krijgslaan 281-S9, B-9000 Gent, Belgium*
[4]*Department of Physics and Astronomy, Louisiana State University, Baton Rouge, LA 70803, USA*
[5]*School of Physics and Astronomy, Cardiff University, Cardiff, Wales CF24 3AA, UK*

Accepted 2022 November 25. Received 2022 November 4; in original form 2022 June 1

ABSTRACT

Core-collapse supernovae (CCSNe) are capable of producing large quantities of dust, with strong evidence that ejecta dust masses can grow significantly over extended periods of time. Red–blue asymmetries in the broad emission lines of CCSNe can be modelled using the Monte Carlo radiative transfer code DAMOCLES, to determine ejecta dust masses. To facilitate easier use of DAMOCLES, we present a Tkinter graphical user interface (GUI) running DAMOCLES. The GUI was tested by high school students through the Original Research By Young Twinkle Students programme, who used it to measure the dust masses formed at two epochs in Type IIP CCSNe, SN 2012aw and iPTF14hls, demonstrating that a wide range of people can contribute to scientific advancement. Bayesian methods quantified uncertainties on our model parameters. From the red scattering wing in the day 1863 Hα profile of SN 2012aw, we constrained the dust composition to large (radius $>0.1\,\mu$m) silicate grains, with a dust mass of $6.0^{+21.9}_{-3.6} \times 10^{-4}$ M$_\odot$. From the day 1158 Hα profile of SN 2012aw, we found a dust mass of $3.0^{+14}_{-2.5} \times 10^{-4}$ M$_\odot$. For iPTF14hls, we found a day 1170 dust mass of $8.1^{+81}_{-7.6} \times 10^{-5}$ M$_\odot$ for a dust composition consisting of 50 per cent amorphous carbon and 50 per cent astronomical silicate. At 1000 d post-explosion, SN 2012aw and iPTF14hls have formed less dust than the peculiar Type II SN 1987A, suggesting that SN 1987A may have formed a larger dust mass than typical Type IIP's.

Key words: supernovae: individual: SN 2012aw, iPTF14hls – dust, extinction – ISM: supernova remnants.

1 INTRODUCTION

The presence of large amounts of dust in high-redshift young galaxies (e.g. Bertoldi et al. 2003; Watson et al. 2015; Laporte et al. 2017) challenged the longstanding assumption that most cosmic dust in the Universe was formed by asymptotic giant branch stars, which mostly form dust on long evolutionary time-scales. It has long been known that dust can form in the ejecta of core-collapse supernovae (CCSNe) and Morgan & Edmunds (2003) and Dwek, Galliano & Jones (2007) have estimated that each CCSN would need to produce $\geq$0.1 M$_\odot$ of dust for CCSNe to be the main dust producers in the Universe. Such yields have been predicted theoretically (e.g. Nozawa et al. 2003; Sarangi & Cherchneff 2015).

It is well known that CCSNe can form large amounts of dust. Fits to the spectral energy distributions (SEDs) of warm dust emitting at mid-infrared (IR) wavelengths as measured with the *Spitzer Space Telescope* found dust masses of only around 10^{-4}–10^{-2} M$_\odot$ (Sugerman et al. 2006; Rho et al. 2009; Fabbri et al. 2011). However, Matsuura et al. (2011) found a cold dust mass of $\sim$0.5 M$_\odot$ from measurements of the far-IR SED of SN 1987A taken with the *Herschel Space Observatory* 23 yr after outburst. Subsequent analyses of *Herschel* far-IR data for Cas A and other SN remnants have detected large cold dust masses between 0.04 and 1.0 M$_\odot$ (Gomez et al. 2012; De Looze et al. 2017, 2019; Temim et al. 2017; Chawner et al. 2019; Priestley, Barlow & De Looze 2019; Niculescu-Duvaz et al. 2021).

In order to provide a method for measuring SN dust masses that would not rely on infrared SED measurements, Bevan & Barlow (2016), motivated by the work of Lucy et al. (1989) on SN 1987A, developed the Monte Carlo radiative transfer code DAMOCLES, which quantifies the amount of newly formed dust causing the absorption and scattering of CCSN ejecta line emission by modelling observed red–blue line asymmetries. The effect is caused by light from the receding redshifted side of a CCSN being attenuated by more internal dust than light from the approaching blueshifted side.

★ E-mail: mjb@star.ucl.ac.uk

Many authors have noted the presence of red–blue asymmetries in the line profiles of CCSNe (Smith, Foley & Filippenko 2008; Mauerhan & Smith 2012; Milisavljevic et al. 2012; Gall et al. 2014). Dust mass measurements of SN 1987A between 714 and 3604 d by Bevan & Barlow (2016) using DAMOCLES were in agreement with the work of Wesson et al. (2015), who modelled its IR SEDs at similar epochs, both finding that by day 3604 the dust mass in SN 1987A had reached $\sim$0.1 $M_\odot$, and that the dust mass increase with time could be fitted with a sigmoid function. DAMOCLES has since been applied to other objects such as SN 1980K, SN 1993J, Cas A (Bevan, Barlow & Milisavljevic 2017), and SN 2005ip (Bevan et al. 2019), with all these objects being found to have dust masses $>$0.1 $M_\odot$. Niculescu-Duvaz et al. (2022) used DAMOCLES to model the multi-epoch optical spectra of 13 CCSNe aged between 5 and 60 yr, compiling the most comprehensive set of very late epoch CCSN ejecta dust measurements made to date. They confirmed that, on average, the dust mass growth could be fitted by a sigmoid curve, saturating on a time-scale of $\sim$30 yr at a value of $0.42^{+0.09}_{-0.05}$ $M_\odot$.

However, there are not yet enough CCSN dust mass estimates available to be able to discern correlations between dust mass, grain size, and CCSN properties such as SN sub-type and progenitor mass. In this work, we aim to add to the sample of CCSNe that have derived dust masses with robustly quantified uncertainties across a range of epochs. We also try, where possible, to constrain the dust grain size and composition. These parameters can help constrain reverse shock dust destruction rates, which have been deduced to range between 0 and 100 per cent (Nath, Laskar & Shull 2008; Silvia, Smith & Shull 2010; Bocchio, Jones & Slavin 2014; Micelotta, Dwek & Slavin 2016; Kirchschlager et al. 2019; Kirchschlager, Barlow & Schmidt 2020; Slavin et al. 2020; Priestley et al. 2021), and which are strongly dependent on the properties adopted for the dust.

In this paper, we present late epoch (days 752 to 1863) optical spectra of two Type IIP CCSNe, SN 2012aw and iPTF14hls. Both show pronounced red–blue line asymmetries, with blueshifted emission peaks attributable to internal dust attenuating more light from the redshifted far side of the ejecta than from the blueshifted near side. From spectropolarimetry of SN 2012aw obtained between days 16 and 120 after outburst, a period when the optical line profiles still showed P Cygni profiles, Dessart et al. (2021) deduced the presence of significant asymmetry in its ejecta. If ejecta asymmetries played a major role in shaping later epoch emission-line profiles, then we might expect to encounter equal numbers of CCSNe showing blueshifted or redshifted emission-line peaks. In fact, the late epoch spectral study by Niculescu-Duvaz et al. (2022) found only blueshifted emission-line peaks among their sample. SN 1941C, observed in 2019 by Fesen & Weil (2020), is a rare example of a CCSN showing a net redshifted late epoch emission-line profile.

Section 2 describes the Original Research By Young Twinkle Students (ORBYTS) programme, through which part of this work was done, while Section 3 summarizes the optical spectra of SN 2012aw and iPTF14hls modelled in this paper. There is no particular motivation behind the selection of these two CCSNe: iPTF14hls was found by students during an exercise searching through the WISeREP archive to find objects with broad-line emission, and SN 2012aw was randomly chosen for students to model from the Gemini GMOS and X-Shooter late-time CCSNe survey presented in Wesson et al. (in preparation). It exhibited a fairly smooth and uncomplicated line model, which was ideal for testing the graphical user interface (GUI). Section 4 outlines the DAMOCLES code and the methodology used to model the observed emission lines, whereas Section 5 describes a GUI wrapper written for DAMOCLES to facilitate a more efficient and clear modelling process, which was deployed through the ORBYTS programme. Sections 6 and 7 present the results of our models of the Hα line in SN 2012aw and iPTF14hls, and in Section 8 we present our conclusions.

2 ORIGINAL RESEARCH BY YOUNG TWINKLE STUDENTS (ORBYTS)

ORBYTS is a National Educational Opportunities Network award-winning educational programme managed by Blue Skies Space Ltd. and University College London (UCL), in which secondary school pupils work on original research under the tutelage of PhD students and other young scientists (McKemmish et al. 2017b; Sousa-Silva et al. 2018).

As part of the ORBYTS scheme, researchers pay fortnightly visits to their partner school over the academic year and facilitate cutting-edge research. One of the core aims of the programme is to address the underrepresentation of people from socially deprived backgrounds in higher education. Longitudinal schemes are the most effective way to increase pupil interest in taking Science, Technology, Engineering, and Mathematics (STEM) subjects at university (Simon, Mallaburn & Seton 2020). The ORBYTS programme achieves this goal by improving pupils' confidence in their abilities through regular interaction with their tutor, which changes the narrative on what it means to be a scientist.

ORBYTS spans a wide range of research areas, such as providing accurate molecular transition frequencies ((McKemmish et al. 2017a, 2018; Chubb et al. 2018; Darby-Lewis et al. 2019)) and characterizing the transit parameters of a range of exoplanets (Edwards et al. 2020, 2021). Other projects have included analysing CH_3OH and CH_3CHO emission in protostellar outflows (Holdship et al. 2019), applying of artificial intelligence to images (Francis et al. 2020), X-ray spectral analysis of active galactic nuclei (Grafton-Waters et al. 2021), and planetary aurorae (Wibisono et al. 2020).

In this work, students partook in a wide range of research-related tasks, such as searching archival data for SNe with optical broad-line emission, as well as using the DAMOCLES code to model line profiles in CCSNe, with the aim of quantifying parameters of the SN ejecta and the dust masses present.

3 OBSERVATIONS

The optical spectra of SN 2012aw we model in this work were taken with the 8-m Gemini-North telescope, and are part of a Gemini GMOS and Very Large Telescope (VLT) X-Shooter late-time spectroscopic survey of CCSNe presented by Wesson et al. (in preparation). The Gemini GMOS-N spectra cover the range 4400–7500 Å and were obtained on 2015 May 18 and 2017 April 22 in long-slit mode using the B600 grating, with a slit width of 0.75 arcsec. The spectra were taken at two or three central wavelength settings and co-added to prevent important spectral features from falling in detector gaps. The spectra have a resolution of 3.5 Å at a wavelength of 6000 Å. The two-dimensional (2D) spectra were bias-corrected, flat-fielded, and wavelength calibrated using the IRAF *gemini* package, and corrected for cosmic rays using the LACOS package of Van Dokkum (2001). The sky subtraction regions were determined by visual inspection and the spectra were extracted using 15 rows centred on the SN's position. Plots of the Gemini spectra are shown in Fig. A1 of Appendix A.

We retrieved two spectra of iPTF14hls from the WISeREP archive.[1] The first was taken on 2016 November 8 by Sollerman et al.

[1] https://wiserep.weizmann.ac.il/

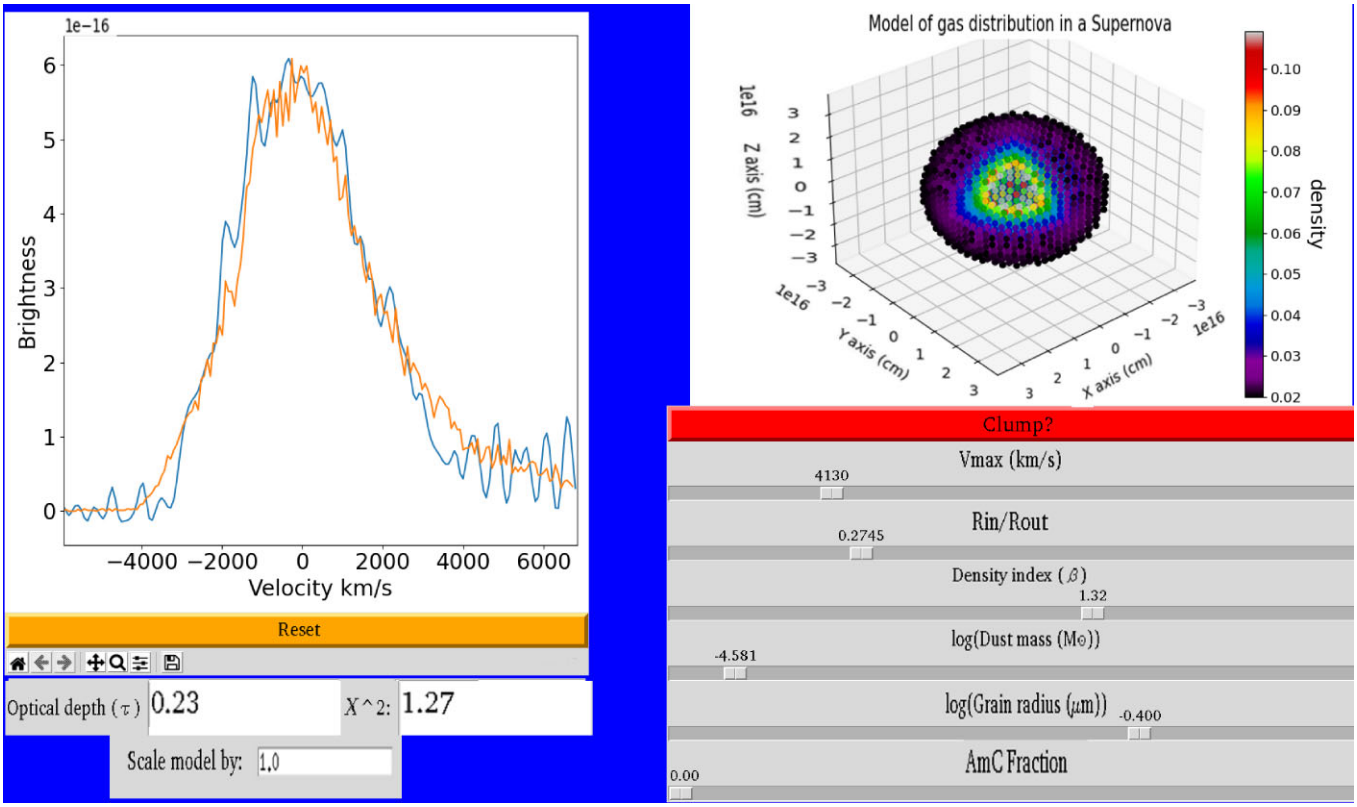

Figure 1. The Tkinter GUI used to explore the parameter space of DAMOCLES models in this work.

(2019) with the low-dispersion spectrograph FLOYDS on the LCO Haleakala (FTN) telescope. The spectrum has a wavelength range of 4000–9300 Å and a resolution of 10 Å. The second spectrum was taken on 2018 January 14 by Sollerman et al. (2019) with the low-resolution instrument on the Keck I telescope. The spectral range is 3070–10265 Å, with a resolution of ∼5 Å. More observational details of the spectra can be found in the referenced literature; plots of the two spectra are shown in Fig. A2 of Appendix A.

4 METHODOLOGY

All models of the CCSNe presented in this work were created with the Monte Carlo radiative transfer code DAMOCLES, which was initially presented and described in depth by Bevan & Barlow (2016). DAMOCLES is written in FORTRAN 95 and parallelized with OPENMP (Dagum & Menon 1998). It models the scattering and absorption of emission line photons by dust in an expanding ejecta. It has been benchmarked against analytical models of theoretical line profiles based on work by Gerasimovic (1933), and also against numerical models of SN 1987A made by Lucy et al. (1989). DAMOCLES is a versatile code able to treat any arbitrary dust/gas geometry, as well as a range of velocity and density distributions and dust and gas clumping configurations. It can also handle a wide range of dust species and grain radii.

Our approach to modelling the line profiles is described for SN 1987A by Bevan & Barlow (2016), and for a range of CCSNe by Niculescu-Duvaz et al. (2022). The parameter space was first examined manually using a GUI, which is described in Section 5, to find the best-fitting model. All models had five free parameters: the outer expansion velocity $V_{\rm max}$, the emitting shell radius ratio $R_{\rm in}/R_{\rm out}$, the density profile index β, where $\rho \propto r^{-\beta}$, the dust mass $M_{\rm d}$, and grain radius a. We determined $V_{\rm max}$ from the point at which the observed flux vanishes on the blueshifted part of the line profile, as the red wing of the profiles can be modified due to dust scattering. $R_{\rm in}/R_{\rm out}$ was set so the model line profile matched the blueshifted peak in the observed profile and its matching redshifted inflection point. The density profile β is identified from the gradient of the emission-line profile wings. After these values are fixed, we then iterate over the grain radius and dust mass to fit the observed profile.

We assume that at the epochs considered here the line-emitting gas is optically thin, and that the emissivity distribution is proportional to the square of the local gas density. The gas is kept smoothly distributed for all models. As the modelled CCSNe are young, we assume that the SN ejecta is in free expansion, such that $V_{\rm max} = R_{\rm out}/t$, where t is the age of the SN. The dust and the gas are co-located in our simulations, such that the dust and the gas have the same $V_{\rm max}$ and $R_{\rm in}/R_{\rm out}$, and, for smoothly distributed dust models, the gas and the dust have the same β values. The dust in our models consists of amorphous carbon (AmC), silicates, or a 50:50 mix of both.

Occasionally, there can be a particularly pronounced red scattering wing in an observed line profile, which requires a dust species with an albedo >0.7 to produce an adequately fitting model. In this case, we can constrain the dust species in our model to be silicate dust with a grain radius between 0.1 and 1.0 μm, as only these grain configurations provide a large enough albedo. We use 'astronomical silicate' as the silicate dust species, with the optical constants of Draine & Lee (1984), along with the BE AmC optical constants of Zubko et al. (1996).

We modelled the line profiles first using a smooth and then a clumped dust distribution, where the radius of an individual clump is $R_{\rm out}/40$. We prefer the dust masses derived for a clumped distribution over a smooth one. This is due to the fact that models of early

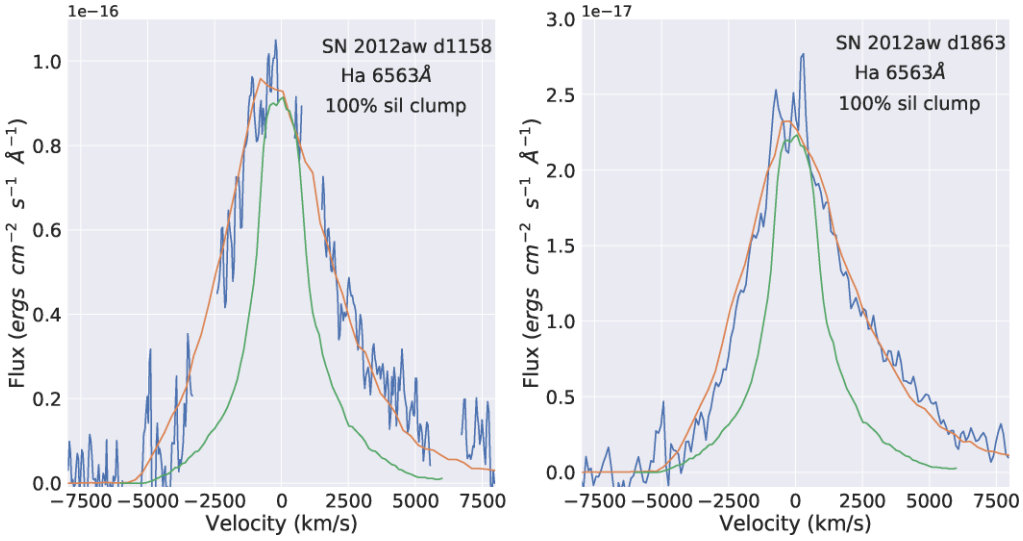

Figure 2. Dust-affected DAMOCLES models for the Hα profile (orange line) of SN 2012aw in Gemini GMOS spectra (blue) taken 1158 (left) and 1863 d (right) post-explosion. The green line is the dust-free model, normalized to the peak level of the observed profile. Clumped dust models corresponding to 100 per cent astronomical silicate are shown.

observations of SN 1987A required dust to be present in optically thick clumps (Lucy et al. 1989, 1991; Bouchet et al. 1996; Kozma & Fransson 1998). Similarly to the work of Niculescu-Duvaz et al. (2022), we fixed the clump distribution power-law index to be 3 and the clump volume filling factor to be 0.1. We note that clumped dust models display less of a scattering wing and attenuate the red wing of the line profile less than smooth dust models, given no change in the other model parameters between the two cases. When the dust is located in clumps, impacting radiation is subject to less scattering as well as to less absorption. So, for a clumped dust model to match the line profile generated by a smooth dust model, a small modification to the grain radius to produce a larger albedo, as well as a dust mass larger by a factor of $\sim$2 than for the smooth case, are required.

We conducted a Bayesian analysis on every emission-line profile modelled in this work, so as to quantify errors on the model parameters. We use the Bayesian approach to modelling line profiles with DAMOCLES first described by Bevan (2018). We use an affine invariant Markov chain Monte Carlo ensemble sampler, EMCEE (Goodman & Weare 2010; Foreman-Mackey et al. 2013) with DAMOCLES to sample the posterior probability distribution of the input parameters. This is defined by Bayes' theorem, presented in equation (1):

$$P(\theta|D) \propto P(\theta)P(D|\theta). \tag{1}$$

In this equation, D is the data, θ is the set of parameters of the model, $P(\theta)$ is our prior understanding of the probability of the parameters, and $P(D|\theta)$ is the likelihood, which is the probability of obtaining the data for a given set of parameters. The likelihood function we used is proportional to $\exp(-\chi^2_{\rm red})$, where $\chi^2_{\rm red} = \chi^2/\upsilon$, and υ is the number of degrees of freedom and χ^2 is defined by equation (2):

$$\chi^2 = \sum_{i=1}^{n} \frac{(f_{{\rm mod},i} - f_{{\rm obs},i})^2}{\sigma_i^2}, \tag{2}$$

where $f_{{\rm mod},i}$ is the modelled flux in bin i, $f_{{\rm obs},i}$ is the observed flux in frequency bin i, and σ_i is the combined Monte Carlo and observational uncertainty in bin i. The modelled line profile from which $f_{{\rm mod},i}$ is taken is normalized to the peak flux of the observed line profile. Priors for each model are given in uniform space, with the exception of the dust mass and grain radius, which are given in log-uniform space as their possible values can span several magnitudes.

Final posterior probability distributions for our input parameters are presented as a series of 2D contour plots, where each pair of parameters is marginalized over the other parameters. We also present a one-dimensional (1D) marginalized posterior probability distribution for each parameter. The 'best-fitting' parameter value found from the Bayesian analysis is given as the median of the marginalized 1D probability distribution. The mean was not used as many probability distributions deviated from a Gaussian distribution. The lower and upper limits were taken to be the 16th and 84th quartiles for the 1D posterior probability distributions. The Bayesian model fits presented in this work all use a 100 per cent clumped silicate dust composition. In the case of iPTF14hls, to find uncertainties on the dust mass for a 50:50 AmC-to-silicate-dust ratio, we find the percentage errors on the manually determined dust mass from the limits determined by the Bayesian analysis for a 100 per cent silicate composition and scale them to that value.

As we had to run many models, we restricted our parameter space to five dimensions, representing the parameters described earlier. Our parameter space was explored by 250 walkers. For each parameter, the number of iteration steps for the autocorrelation function to initially decay down towards zero is roughly one autocorrelation time. We checked that each model was run for five or more autocorrelation times to ensure convergence. The acceptance fraction is the fraction of times the EMCEE algorithm has accepted a new proposed set of values. An acceptable value of the acceptance fraction is between 0.2 and 0.5 (Gelman, Roberts & Gilks 1996). For each simulation, our acceptance fraction averaged at around 0.3.

5 THE INTERACTIVE DAMOCLES ENVIRONMENT

Here, we describe the GUI we created, which was tested through the ORBYTS programme where students used it to find the best-fitting DAMOCLES models of the Hα line profiles of SN 2012aw and iPTF14hls. This interactive environment provides a user-friendly way to manually explore parameter space and investigate how each

Table 1. Parameters used in the DAMOCLES models, found from a manual examination of parameter space, of the broad emission lines of SN 2012aw and iPTF14hls for spherically symmetric smooth and clumped dust models. The '% Sil' column stands for percentage of the dust species that is astronomical silicate, where the remainder of the dust is AmC dust. The optical depth τ is calculated from $R_{\rm in}$ to $R_{\rm out}$ for a central line wavelength for Hα of 6563 Å. The columns labelled + and − represent the upper and lower uncertainties on the dust mass, such that the maximum possible dust mass is $M_{\rm dust}$ added to the corresponding value listed in the + column, and the minimum possible dust mass is the corresponding value in the − column subtracted from $M_{\rm dust}$. These limits are derived from the 16th and 84th quartiles on the median value of the 1D posterior probability density function (PDF) for the dust mass found from a Bayesian simulation, and are scaled as a percentage error to the reported values of $M_{\rm dust}$ in this table.

SN	Line	Epoch (d)	Clumped	% Sil	a (μm)	$V_{\rm max}$ (km s^{-1})	$V_{\rm min}$ (km s^{-1})	$\beta_{\rm gas}$	$R_{\rm out}$ 10^{13} cm	$R_{\rm in}$ 10^{13} cm	$M_{\rm dust}$ 10^{-4} M$_\odot$	+ 10^{-4} M$_\odot$	− 10^{-4} M$_\odot$	τ
2012aw	Hα	1158	No	100	0.30	5500	1100	1.30	55.03	11.01	2.0	8.9	1.6	0.70
2012aw	Hα	1158	Yes	100	0.30	5500	1100	1.30	55.03	11.01	2.0	8.9	1.6	0.70
2012aw	Hα	1158	No	75	0.25	5500	1100	1.30	55.03	11.01	1.5	6.6	1.2	0.64
2012aw	Hα	1158	Yes	75	0.25	5500	1100	1.30	55.03	11.01	1.0	4.4	0.8	0.43
2012aw	Hα	1863	No	100	0.30	5100	663	1.53	82.09	10.67	7.0	25.5	4.2	1.19
2012aw	Hα	1863	Yes	100	0.30	5100	663	1.53	82.09	10.67	6.0	21.8	3.6	1.02
2012aw	Hα	1863	No	75	0.25	5100	663	1.60	82.09	10.67	5.0	18.2	3.0	1.03
2012aw	Hα	1863	Yes	75	0.25	5100	663	1.60	82.09	10.67	5.0	18.2	3.0	1.03
iPTF14hls	Hα	752	Yes	0	0.18	4000	1107	1.30	27.2	7.5	0.10	1.20	0.096	0.34
iPTF14hls	Hα	752	No	0	0.15	4000	1107	1.30	27.2	7.5	0.03	0.37	0.029	0.12
iPTF14hls	Hα	752	Yes	100	0.044	4100	1107	1.13	27.2	7.5	0.28	3.5	0.27	0.26
iPTF14hls	Hα	752	No	100	0.057	4100	1107	1.30	27.2	7.5	0.21	2.60	0.20	0.22
iPTF14hls	Hα	752	Yes	50	0.10	4100	1107	1.30	27.2	7.5	0.13	0.12	1.60	0.23
iPTF14hls	Hα	752	No	50	0.09	4100	1107	1.30	27.2	7.5	0.18	0.17	2.2	0.32
iPTF14hls	Hα	1170	Yes	0	0.18	6025	1085	2.30	60.90	10.96	0.47	4.7	0.44	0.34
iPTF14hls	Hα	1170	No	0	0.15	6025	1085	2.30	60.90	10.96	0.46	4.6	0.43	0.40
iPTF14hls	Hα	1170	Yes	100	0.044	6025	1085	2.30	60.90	10.96	18.0	179.4	16.9	0.28
iPTF14hls	Hα	1170	No	100	0.038	6025	1085	2.30	60.90	10.96	18.6	174.3	17.4	0.34
iPTF14hls	Hα	1170	Yes	50	0.10	6025	1085	2.30	60.90	10.96	0.81	8.1	0.76	0.33
iPTF14hls	Hα	1170	No	50	0.10	6025	1085	2.30	60.90	10.96	0.61	6.1	0.57	0.26

parameter affects the input model. It has been made public on GitHub.[2] It is written in PYTHON using the Tkinter package, and uses the FORTRAN to PYTHON interface generator F2PY3 to run the DAMOCLES code from the GUI. Upon running the GUI, the user is first prompted to enter relevant information, e.g. the wavelength of the emission line of interest and the filename and epoch of the observed data. Upon completion of the necessary fields, the main window where DAMOCLES models are created is spawned. The layout of this window can be seen in Fig. 1. The user sets the parameters of the gas and dust CCSN model via sliders. There are sliders for $V_{\rm max}$, $R_{\rm in}/R_{\rm out}$, the density profile index β, the dust mass ($M_{\rm d}$), grain radius (a), and the fraction of AmC to silicate dust. When a slider is moved to a desired value, the current values of each slider are set in the input files of DAMOCLES. The user can push the red button above the sliders if they want to switch from a smooth dust distribution to a clumped one. The default filling factor for the clumped dust model is 0.1, where the power-law index for the clump number density distribution is 3.0. The model three-dimensional gas shell for the CCSN is then generated and plotted in the upper right pane. This is useful for visual purposes, as it informs the user of how changing a parameter affects the distribution of gas in the model. DAMOCLES is called to run within the GUI using the parameters specified by the user. The output line profile generated by DAMOCLES is overplotted on to the observed line profile in the left-hand pane. The χ^2 value between the model and observed line profile is provided below this pane, as is the radial optical depth, τ, of the dust shell between $R_{\rm in}$ and $R_{\rm out}$.

[2]https://github.com/damocles-code/damocles

6 SN 2012AW

SN 2012aw in the galaxy M 95 was discovered on 2012 March 16 by Fagotti et al. (2012). Observations of M 95 a day earlier (Poznanski et al. 2012), with a limiting magnitude of $R > 20.7$, did not detect the SN, so the explosion date can be well constrained to 2012 March 16. Bose et al. (2013) classified it as Type IIP from fitting the light curve of the archetypal Type IIP SN 1999em to photometric points taken 4–270 d after the explosion date. The relative proximity of M 95, as well as the relatively low dust extinction towards it, meant that SN 2012aw was the first SN to have a plateau detected in its ultraviolet light curve (Bayless et al. 2013).

The progenitor mass of SN 2012aw has been estimated by several authors. Van Dyk et al. (2012) detected the near-IR signal of a progenitor in archival data taken 6–12 yr before explosion, as well as an optical signal 17–18 yr before, from archival *HST* data. They estimated that the progenitor was likely a red supergiant, with a progenitor mass of 17–18 M$_\odot$, from fitting the observed IR SED with synthetic photometry from a MARCS model stellar atmosphere and then comparing the derived $T_{\rm eff}$ and luminosity to theoretical massive star evolutionary tracks. They also estimated a high visual extinction in front of the progenitor star ($A_{\rm V} = 3.1$ mag), much higher than the post-explosion estimate ($A_{\rm V} = 0.24$ mag), which they interpreted as implying the destruction of a large amount of circumstellar dust by the explosion. Jerkstrand et al. (2014) obtained optical spectra 250–451 d after explosion and near-IR spectra 306 d after explosion. From spectral synthesis models to their data, they constrained the progenitor mass of SN 2012aw to be 14–18 M$_\odot$. Fraser (2016) independently estimated the progenitor mass to be 12.5 ± 1.5 M$_\odot$.

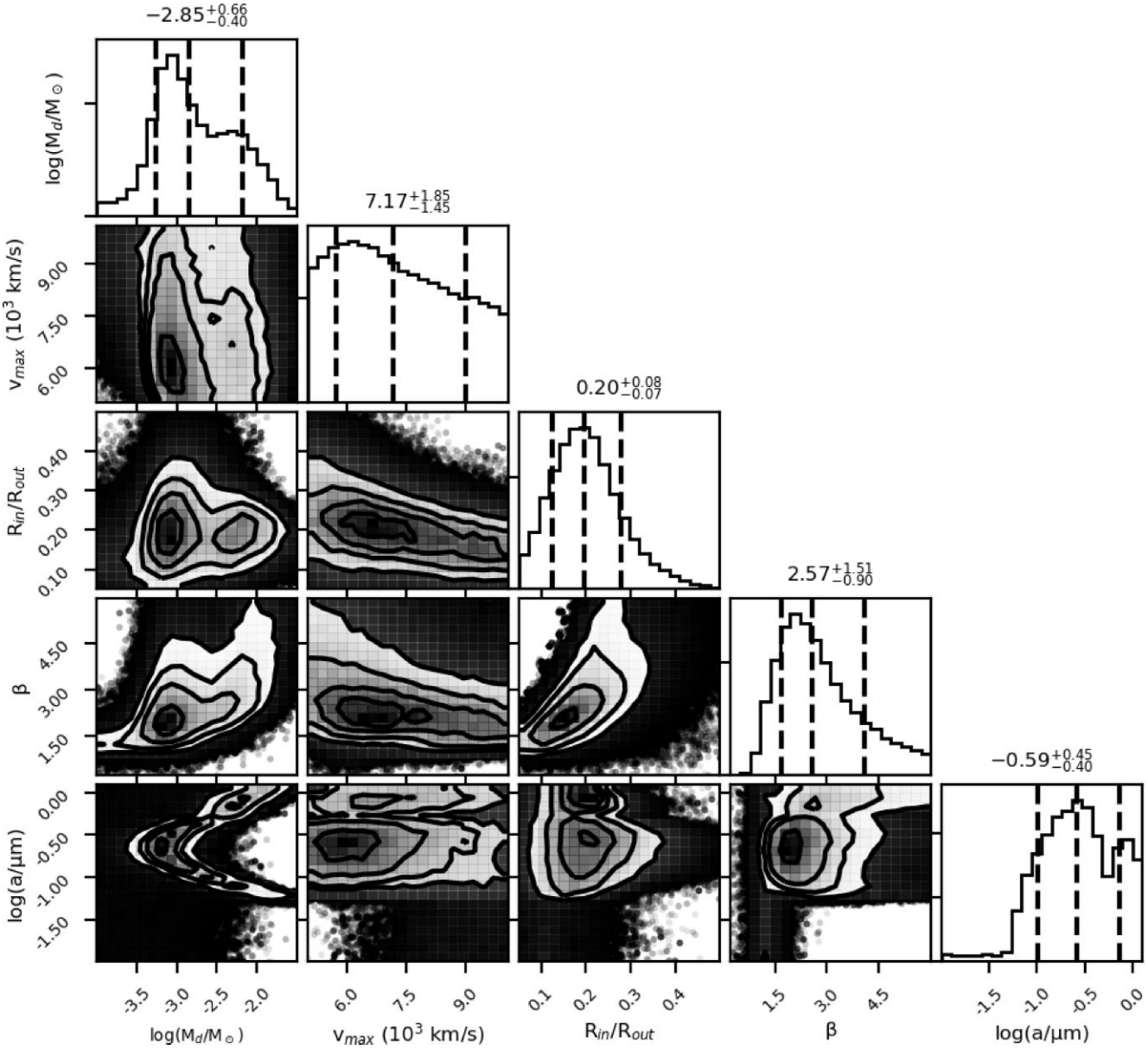

Figure 3. The full posterior probability distribution for the 5D model of SN 2012aw's Hα profile at day 1863, using a 100 per cent silicate dust composition. The contours of the 2D distributions represent 0.5σ, 1.0σ, 1.5σ, and 2.0σ and the dashed, black vertical lines represent the 16th, 50th, and 84th quartiles for the 1D marginalized probability distributions.

ORBYTS pupils used the GUI applet described in Section 5 to find a best-fitting model of the Hα line profile in our GMOS spectra of SN 2012aw taken at 1158 and 1863 d past explosion, by reducing the χ^2 value. The spectra were corrected for an M 95 recessional velocity of 779 km s^{-1} (Springob et al. 2005). Models were convolved to the spectral resolution of the GMOS instrument using a Gaussian kernel. Best-fitting models are shown in Fig. 2 and the model parameters are listed in Table 1. Models made using amorphous carbon as the dust grain species failed to replicate the pronounced red scattering wing, and at both epochs, we were unable to achieve a good fitting model to the Hα profile using a silicate-to-carbon ratio of less than 0.75. From a manual fitting process, we were able to constrain the grain radius at both epochs to be $\sim$0.3 μm for a 100 per cent silicate dust composition.

We quantified the uncertainties on the input parameters at both epochs using a Bayesian analysis with a 100 per cent silicate dust composition, the corner plot for which can be seen in Fig. 3. Grain radii smaller than 0.1 μm were strongly ruled out, while the median grain radius of $0.25^{+0.47}_{-0.15}$ μm that was found was very close to the value of 0.3 μm found from manually fitting the line profile, while the dust masses we determined manually of $6.0^{+21.9}_{-3.6} \times 10^{-4}$ M$_\odot$ also fell within the limits determined by the Bayesian analysis.

From a Bayesian analysis, we found a lower median dust mass for SN 2012aw at day 1158, 3.0×10^{-4} M$_\odot$, very close to our initial estimate of $2.0^{+8.9}_{-1.6} \times 10^{-4}$ M$_\odot$, but the grain size was not as well constrained at this earlier epoch. These dust masses have been plotted in the dust mass growth with time plot shown in figs 22 and 23 of Niculescu-Duvaz et al. (2022).

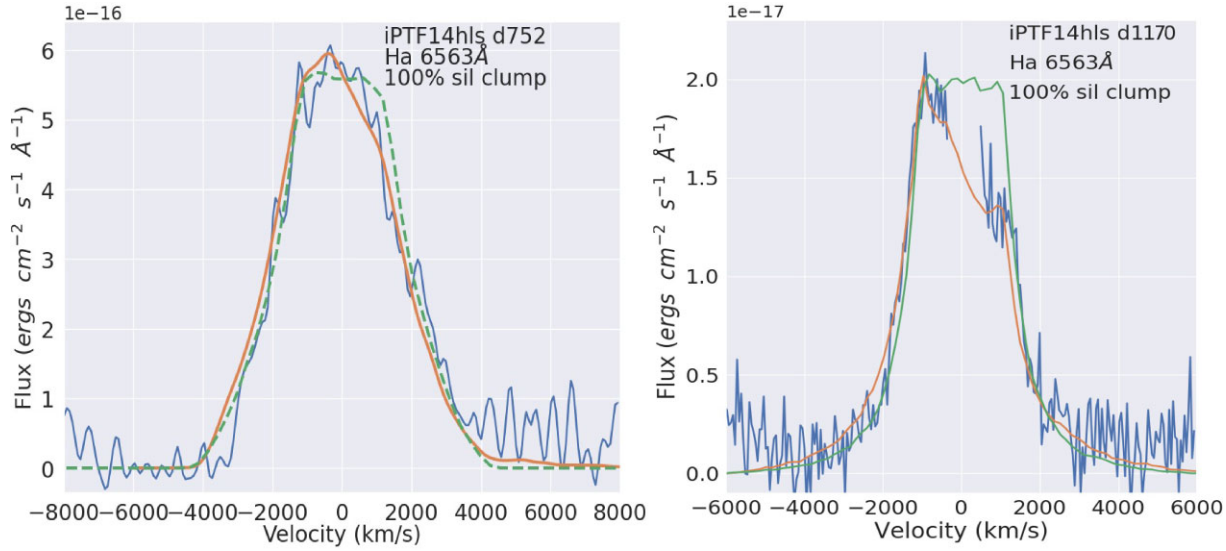

Figure 4. Dust-affected DAMOCLES models (orange lines) for the observed (blue) Hα line profiles of iPTF14hls at 752 (left) and 1170 d (right) post-explosion. The green lines are the dust-free models, normalized to the peak levels of the observed profiles. Clumped dust models corresponding to 100 per cent astronomical silicate are shown.

7 IPTF14HLS

iPTF14hls was discovered on 2014 September 22 by the intermediate Palomar Transient Factory (iPTF) wide-field camera survey (Arcavi et al. 2017). We adopt their discovery date as the explosion date, as well as the redshift (z) of 0.0344 they determined from narrow host-galaxy features. iPTF14hls was classified as an SN of Type IIP by Li, Wang & Zhang (2015) from the broad P Cygni Balmer series lines in an optical spectrum taken on 2015 January 8. iPTF14hls is an unusual SN: peaking at $r = -19.1$ (Sollerman et al. 2019), its light curve as observed by Arcavi et al. (2017) showed five distinct peaks over the first 600 d after explosion. The spectra resembled those of other hydrogen-rich SNe such as SN 1999em, but notably evolved at a much slower pace. Sollerman et al. (2019) continued to monitor the light curve until day 1200, and noted a steep decline in the light curve around day 1000. They also obtained several optical spectra between days 713 and 1170. Yuan et al. (2018) detected a variable γ-ray source with the Fermi Large Area Telescope at a time and position consistent with iPTF14hls, and follow-up work by Prokhorov, Moraghan & Vink (2021) strengthened this association.

A number of authors have attempted to interpret the mechanism inducing the properties exhibited by iPTF14hls. Arcavi et al. (2017) and Chugai (2018) suggested iPTF14hls to have had a massive progenitor that prior to explosion underwent extreme mass-loss, possibly caused by the pulsational pair-instability mechanism. Dessart (2018) reproduced most of the observed properties of iPTF14hls with their model of a typical Type II SN created by an H-rich blue supergiant explosion and powered by a magnetar. Andrews & Smith (2018) interpreted the day 1153 optical spectrum as showing clear signs of circumstellar material (CSM)–ejecta interaction, and proposed a set-up for iPTF14hls where an asymmetric disc or torus of CSM was overrun and hidden below the photosphere of the expanding SN ejecta, whereby variations in the density structure of the CSM could explain the multiple peaks in the light curve. Moriya, Mazzali & Pian (2020) and Uno & Maeda (2020) proposed that iPTF14hls was not an SN, but that it could have been an $\sim$100 $M_\odot$ star experiencing variable mass-loss episodes similar to η Carinae, or a binary system of two $\sim$100 $M_\odot$ stars experiencing a dynamical common-envelope evolution. Soker & Gilkis (2018) posited that iPTF14hls consisted of a binary system where a neutron star spiraling inside a massive stellar envelope accreted mass and launched jets that ejected the circumstellar shell and eventually resulted in a final SN explosion.

The Hα line profile in iPTF14hls was modelled by ORBYTS pupils at two epochs (752 and 1170 d after explosion) using DAMOCLES. We do not model the [Ca II] 7330 Å doublet, despite a strong detection at day 1170, as there could be potential contamination from the [O II] 7319, 7330 Å doublet. While the [O I] 6300, 6363 Å line is also visible at this epoch, we considered it to have too low a signal-to-noise ratio to model. All models were convolved using a Gaussian kernel to the spectral resolution of the instrument used to collect the observed data. Contaminating narrow-line emission was removed from the Hα line profile. The day 752 and day 1170 Hα line profile fits, determined from a manual exploration of parameter space, are shown in Fig. 4. The model parameters for both epochs can be found in Table 1.

Bayesian simulations were run for both epochs to constrain the uncertainty limits on the dust mass. The resulting corner plot for the Bayesian simulation of the Hα profile at day 1170 can be found in Fig. 5. At both epochs, the median dust mass found by a Bayesian exploration of parameter space and the best-fitting dust mass that minimized the χ^2 found by a manual-fitting process are within the uncertainty limits derived from the 1D dust mass posterior probability distribution, for a 100 per cent clumped silicate dust distribution. As the dust species could not be determined, we report a final dust mass at day 1170 of $8.1^{+81}_{-7.6} \times 10^{-5}$ $M_\odot$ for a 50:50 AmC-to-amorphous silicate dust ratio, both fixed with a dust grain radius of 0.1 μm that is required to achieve a better fit to the line profile. At both epochs, the lack of a red scattering wing and the relatively low signal to noise of the Hα line profiles meant that we were unable to constrain the dust grain radius. Therefore, the dust mass derived for this grain radius can be seen as a lower limit, as silicate grains smaller than 0.1 μm have a poor extinction efficiency, as do larger carbon grains, such that smaller or larger grains require more dust to produce the same optical depth.

The ejecta dust mass found for SN 1987A at day 1153 from modelling the optical–infrared SED with a clumped AmC dust distri-

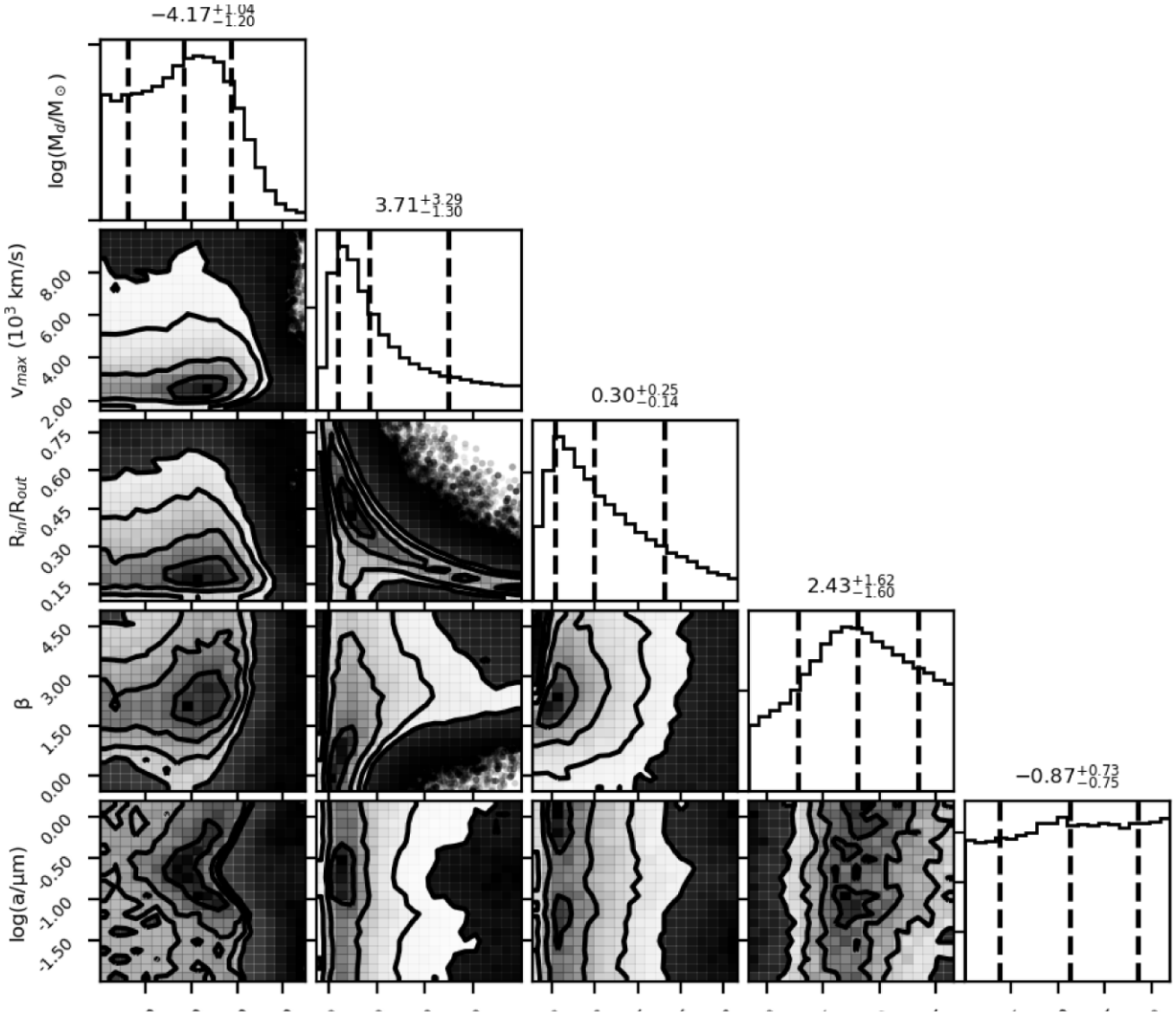

Figure 5. The full posterior probability distribution for the 5D model of the iPTF14hls Hα profile at day 1170, using a 100 per cent clumped silicate dust composition. The contours of the 2D distributions represent 0.5σ, 1.0σ, 1.5σ, and 2.0σ, and the dashed, black vertical lines represent the 16th, 50th, and 84th quartiles for the 1D marginalized probability distributions.

bution was $(3.0 \pm 1.0) \times 10^{-3}$ M$_\odot$ (Wesson et al. 2015), while Bevan & Barlow (2016) modelled the day 1054 red–blue asymmetries of the [OI] 6300, 6363 Å doublet using a clumped 100 per cent AmC composition to obtain a dust mass of $3.0^{+2.0}_{-2.25} \times 10^{-3}$ M$_\odot$, nearly two orders of magnitude larger than our 100 per cent AmC dust mass of 4.7×10^{-5} M$_\odot$ for iPTF14hls at day 1170, and outside of the upper limit of 9.4×10^{-5} M$_\odot$ determined from our iPTF14hls measurement.

For our day 752 models for a 50:50 sil:AmC dust mixture and a grain radius of 0.1 μm, we find a very small amount of dust: $1.0^{+14}_{-1.24} \times 10^{-5}$ M$_\odot$. Although consistent with an increase in dust mass between days 752 and 1170, and despite the appearance of an increasing red–blue asymmetry in the Hα line profiles between those dates, the uncertainties on the dust masses found using Bayesian methods are large enough that we are unable to definitively conclude that the dust mass has grown between these two epochs.

8 DISCUSSION AND CONCLUSIONS

We have used the Monte Carlo radiative transfer code DAMOCLES to model the late epoch Hα line profiles of two Type IIP SNe, SN 2012aw and iPTF14hls, in order to determine their ejecta dust masses and grain parameters, as well as other ejecta parameters, for epochs corresponding to days 1158 and 1863 for SN 2012aw and to days 752 and 1170 for iPTF14hls. We present a GUI wrapper for the DAMOCLES code, written using the PYTHON T kinter module that facilitates a visual understanding of the code and a quick determination of the best-fitting model to a broad emission-line profile for a range of dust compositions. It can be used by both researchers and for citizen science purposes. We have used this GUI to model the Hα red–blue line asymmetries of the two SNe. We have robustly quantified the errors on the derived model parameters using Bayesian inference.

For SN 2012aw, we constrained the day 1863 dust composition to be >75 per cent silicate with a grain radius of $0.26^{+0.46}_{-0.16}$ μm. Using

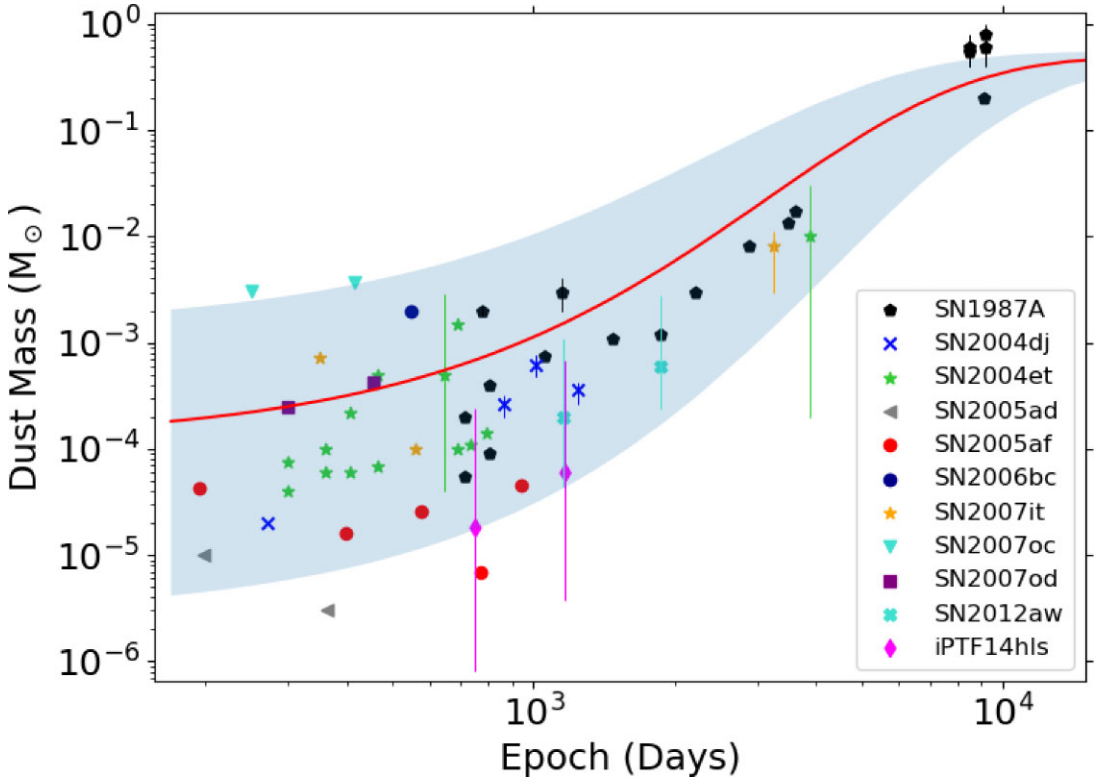

Figure 6. A plot of dust mass versus time since explosion for Type IIP CCSNe with dust mass measurements. Data points for SN 1987A are taken from Matsuura et al. (2011, 2015), Indebetouw et al. (2014), Wesson et al. (2015), Bevan & Barlow (2016), for SN 2004et from Kotak et al. (2009); Fabbri et al. (2011); Niculescu-Duvaz et al. (2022); and for SN 2007it also from Niculescu-Duvaz et al. (2022). The data points for SN 2007oc are from Szalai & Vinkó (2013), from Andrews et al. (2010) for SN 2007od, from Szalai et al. (2011) for SN 2004dj, and from Szalai & Vinkó (2013) for SN 2005ad and SN 2005af. For SN 2006bc, the data are taken from Gallagher et al. (2012). The red sigmoid curve is taken from fig. 23. of Niculescu-Duvaz et al. (2022), where a dust growth trend is fitted to a large sample of CCSN dust mass measurements. The grey band encloses the error region on the best-fitting sigmoid curve parameters, where the errors are derived from a Monte Carlo bootstrap simulation.

this dust composition, the dust mass found for a 100 per cent silicate composition at day 1158 post-explosion was $2.0^{+8.9}_{-1.6} \times 10^{-4}\,M_\odot$, while at day 1863 it was measured to be $6.0^{+21.9}_{-3.6} \times 10^{-4}\,M_\odot$. The large grain radius that we determine for SN 2012aw lends extra weight to the findings of Niculescu-Duvaz et al. (2022) that dust grains in most CCSNe have a grain radius of $>0.1\,\mu$m, which is also in agreement with other studies constraining dust grain sizes (e.g. Gall et al. 2014; Owen & Barlow 2015; Wesson et al. 2015; Bevan et al. 2017; Priestley et al. 2020). Larger dust grains are more likely to survive the passage of the reverse shock than smaller grains, with Slavin et al. (2020) and Kirchschlager et al. (2020, 2022) finding a reverse shock dust destruction rate for silicate grain radii $>0.1\,\mu$m of ∼20–50 per cent.

For iPTF14hls at day 752 we found a dust mass of $1.0^{+14}_{-1.24} \times 10^{-5}\,M_\odot$, while at day 1170, we found a dust mass of $8.1^{+81}_{-7.6} \times 10^{-5}\,M_\odot$ for a dust composition of 50 per cent amorphous carbon and 50 per cent astronomical silicate. The large uncertainty limits on the dust mass measurements for iPTF14hls, and the fact that we could not constrain its dust grain composition, mean that we are unable to be certain that it had formed less dust than SN 2012aw at an epoch of ∼1200 d.

As SN 2012aw and iPTF14hls are fairly bright and young CCSNe, it should be straightforward to conduct follow-up optical observations to monitor the evolution of their dust mass, as they are predicted to have only formed less than 1 per cent of their total dust mass by 1000 d post-explosion (see fig. 23 of Niculescu-Duvaz et al. 2022). An ongoing comparison between the evolution of these CCSNe and SN 1987A would be particularly interesting, as they are all classified as Type IIP CCSNe, but at day ∼1200 both SN 2012aw and iPTF14hls have been found here to have formed less dust than SN 1987A, as can be seen in Fig. 6. At around day 1000 post-explosion, the dust mass measured in SN 2004dj is also less than that found in SN 1987A. This hints that at 1000 d, the peculiar Type II SN 1987A could be an anomalously high-dust former, but more Type IIP SN measurements would need to be made to confirm this for later stages.

ACKNOWLEDGEMENTS

MND, MJB, and RW acknowledge support from European Research Council (ERC) Advanced Grant 694520 SNDUST. IDL acknowledges support from ERC Starting Grant 851622 DustOrigin. WRD acknowledges support from STFC Consolidated Grant ST/S000240/1 to UCL. We also greatly thank both the UCL Widening Participation department and the UKSA Space for all grants for their support of the ORBYTS programme.

DATA AVAILABILITY

Both GUI and Bayesian versions of the DAMOCLES code are made publicly available at https://github.com/damocles-code/damocles. Wavelength-calibrated copies of our Gemini GMOS spectra of SN2012aw are available on the WISeREP archive (https://wiserep.weizmann.ac.il/).

REFERENCES

Andrews J. E., Smith N., 2018, MNRAS, 477, 74
Andrews J. E. et al., 2010, ApJ, 715, 541
Arcavi I. et al., 2017, Nature, 551, 210
Bayless A. J. et al., 2013, ApJ, 764, L6
Bertoldi F., Carilli C. L., Cox P., Fan X., Strauss M. A., Beelen A., Omont A., Zylka R., 2003, A&A, 406, L55
Bevan A., 2018, MNRAS, 480, 4659
Bevan A., Barlow M. J., 2016, MNRAS, 456, 1269
Bevan A., Barlow M. J., Milisavljevic D., 2017, MNRAS, 465, 4044
Bevan A. et al., 2019, MNRAS, 485, 5192
Bocchio M., Jones A. P., Slavin J. D., 2014, A&A, 570, 32
Bose S. et al., 2013, MNRAS, 433, 1871
Bouchet P., Danziger I. J., Gouiffes C., della Valle M., Moneti A., 1996, in Kuhn T. S., ed., IAU Colloq. 145, Supernovae and Supernova Remnants. Cambridge Univ. Press, Cambridge, p. 201
Chawner H. et al., 2019, MNRAS, 483, 70
Chubb K. L. et al., 2018, J. Quant. Spec. Radiat. Transf., 218, 178
Chugai N. N., 2018, Astron. Lett., 44, 370
Dagum L., Menon R., 1998, IEEE Comput. Sci. Eng., 5, 46
Darby-Lewis D. et al., 2019, J. Mol. Spectrosc., 362, 69
De Looze I., Barlow M. J., Swinyard B. M., Rho J., Gomez H. L., Matsuura M., Wesson R., 2017, MNRAS, 465, 3309
De Looze I. et al., 2019, MNRAS, 488, 164
Dessart L., 2018, A&A, 610, L10
Dessart L., Leonard D. C., Hillier D. J., Pignata G., 2021, A&A, 651, A19
Draine B. T., Lee H. M., 1984, ApJ, 285, 89
Dwek E., Galliano F., Jones A. P., 2007, ApJ, 662, 927
Edwards B. et al., 2020, Res. Notes AAS, 4, 109
Edwards B. et al., 2021, MNRAS, 504, 5671
Fabbri J. et al., 2011, MNRAS, 418, 1285
Fagotti P. et al., 2012, CBET, 3054, 1
Fesen R. A., Weil K. E., 2020, ApJ, 890, 15
Foreman-Mackey D., Hogg D. W., Lang D., Goodman J., 2013, PASP, 125, 306
Francis A. et al., 2020, Data, 5, 70
Fraser M., 2016, MNRAS, 456, L16
Gall C. et al., 2014, Nature, 511, 326
Gallagher J. S. et al., 2012, ApJ, 753, 109
Gelman A., Roberts G. O., Gilks W. R., 1996, in Bernardo J. M., Berger J. O., Dawid A. P., Smith A. F. M., eds, Bayesian Statistics. Oxford Univ. Press, Oxford, p. 599
Gerasimovic B., 1933, Z. Astrophysik, 7, 335
Gomez H. L. et al., 2012, AJ, 760, 96
Goodman J., Weare J., 2010, Commun. Appl. Math. Comput. Sci., 5, 65
Grafton-Waters S. et al., 2021, Res. Notes AAS, 5, 172
Holdship J. et al., 2019, ApJ, 880, 138
Indebetouw R. et al., 2014, ApJ, 782, L11
Jerkstrand A., Smartt S. J., Fraser M., Fransson C., Sollerman J., Taddia F., Kotak R., 2014, MNRAS, 439, 3694
Kirchschlager F., Schmidt F. D., Barlow M. J., Fogerty E. L., Bevan A., Priestley F. D., 2019, MNRAS, 489, 4465
Kirchschlager F., Barlow M. J., Schmidt F. D., 2020, ApJ, 893, 70
Kirchschlager F., Schmidt F. D., Barlow M. J., De Looze I., Sartorio N. S., 2022, preprint (arXiv:2210.06763)
Kotak R. et al., 2009, ApJ, 704, 306
Kozma C., Fransson C., 1998, ApJ, 497, 431
Laporte N. et al., 2017, ApJ, 837, L21
Li W., Wang X., Zhang T., 2015, Astron. Telegram, 6898, 1
Lucy L. B., Danziger I. J., Gouiffes C., Bouchet P., 1989, in Tenorio-Tagle G., Moles M., Melnick J., eds, Proc. IAU Colloq. 120, Dust Condensation in the Ejecta of SN 1987A. Springer-Verlag, Berlin, p. 164
Lucy L. B., Danziger I. J., Gouiffes C., Bouchet P., 1991, in Woosley S. E., ed., Supernovae. Springer-Verlag, Berlin, p. 82
Matsuura M. et al., 2011, Science, 333, 1258
Matsuura M. et al., 2015, ApJ, 800, 50
Mauerhan J., Smith N., 2012, MNRAS, 424, 2659
McKemmish L. K., Chubb K. L., Rivlin T., Baker J. S., Gorman M. N., Heward A., Dunn W., Tessenyi M., 2017a, Astron. Geophys., 58, 5.11
McKemmish L. K. et al., 2017b, ApJS, 228, 15
McKemmish L. K. et al., 2018, ApJ, 867, 33
Micelotta E. R., Dwek E., Slavin J. D., 2016, A&A, 590, 65
Milisavljevic D., Fesen R. A., Chevalier R. A., Kirshner R. P., Challis P., Turatto M., 2012, ApJ, 751, 25
Morgan H. L., Edmunds M. G., 2003, MNRAS, 343, 427
Moriya T. J., Mazzali P. A., Pian E., 2020, MNRAS, 491, 1384
Nath B. B., Laskar T., Shull J. M., 2008, ApJ, 682, 1055
Niculescu-Duvaz M., Barlow M. J., Bevan A., Milisavljevic D., De Looze I., 2021, MNRAS, 504, 2133
Niculescu-Duvaz M. et al., 2022, MNRAS, 515, 4302
Nozawa T., Kozasa T., Umeda H., Maeda K., Nomoto K., 2003, ApJ, 598, 785
Owen P. J., Barlow M. J., 2015, ApJ, 801, 141
Poznanski D., Nugent P. E., Ofek E. O., Gal-Yam A., Kasliwal M. M., 2012, Astron. Telegram, 3996, 1
Priestley F. D., Barlow M. J., De Looze I., 2019, MNRAS, 485, 440
Priestley F. D., Barlow M. J., De Looze I., Chawner H., 2020, MNRAS, 491, 6020
Priestley F. D., Chawner H., Matsuura M., De Looze I., Barlow M. J., Gomez H. L., 2021, MNRAS, 500, 2543
Prokhorov D. A., Moraghan A., Vink J., 2021, MNRAS, 505, 1413
Rho J. et al., 2009, in Henning T., Grün E., Steinacker J., eds, ASP Conf. Ser. Vol. 414, Cosmic Dust - Near and Far. Astron. Soc. Pac., San Francisco, p. 22
Sarangi A., Cherchneff I., 2015, A&A, 575, 95
Silvia D. W., Smith B. D., Shull J. M., 2010, ApJ, 715, 1575
Simon S., Mallaburn A., Seton L., 2020, Engaging Learners with Chemistry: Projects to Stimulate Interest and Participation. Chapter 10, Enhancing School Students' Engagement in Chemistry through a University-led Enrichment Programme. Royal Society of Chemistry, USA, p. 192
Slavin J. D., Dwek E., Mac Low M.-M., Hill A. S., 2020, ApJ, 902, 135
Smith N., Foley R. J., Filippenko A. V., 2008, ApJ, 680, 568
Soker N., Gilkis A., 2018, MNRAS, 475, 1198
Sollerman J. et al., 2019, A&A, 621, A30
Sousa-Silva C., McKemmish L. K., Chubb K. L., Gorman M. N., Baker J. S., Barton E. J., Rivlin T., Tennyson J., 2018, Phys. Educ., 53, 015020
Springob C. M., Haynes M. P., Giovanelli R., Kent B. R., 2005, ApJS, 160, 149
Sugerman B. E. et al., 2006, Science, 313, 196
Szalai T., Vinkó J., 2013, A&A, 549, A79
Szalai T., Vinkó J., Balog Z., Gáspár A., Block M., Kiss L. L., 2011, A&A, 527, A61
Temim T., Dwek E., Arendt R. G., Borkowski K. J., Reynolds S. P., Slane P., Gelfand J. D., Raymond J. C., 2017, ApJ, 836, 129
Uno K., Maeda K., 2020, ApJ, 897, 156
Van Dokkum P. G., 2001, PASP, 113, 1420
Van Dyk S. D. et al., 2012, ApJ, 756 9
Watson D., Christensen L., Knudsen K. K., Richard J., Gallazzi A., Michałowski M. J., 2015, Nature, 519, 327
Wesson R., Barlow M. J., Matsuura M., Ercolano B., 2015, MNRAS, 446, 2089
Wibisono A. D. et al., 2020, J. Geophys. Res.: Space Phys., 125, e27676
Yuan Q., Liao N.-H., Xin Y.-L., Li Y., Fan Y.-Z., Zhang B., Hu H.-B., Bi X.-J., 2018, ApJ, 854, L18
Zubko V. G., Mennella V., Colangeli L., Bussoletti E., 1996, MNRAS, 282, 1321

APPENDIX

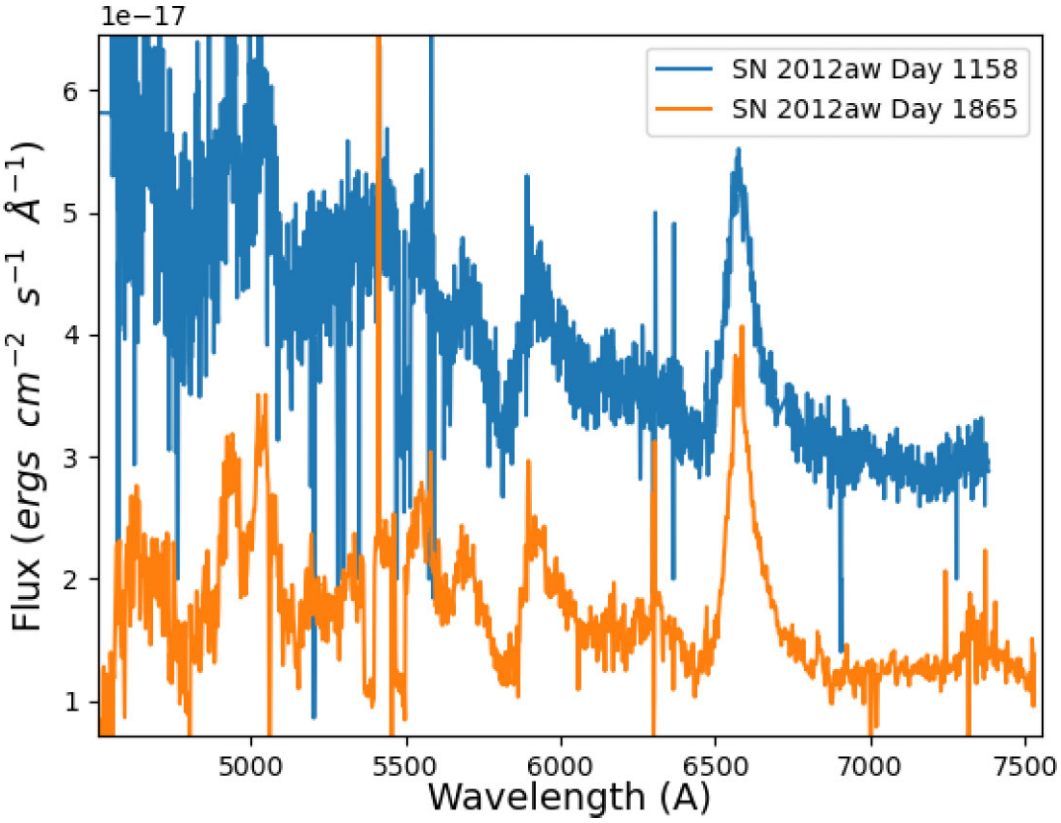

Figure A1. The evolution of the optical spectrum of SN 2012aw. Information on the spectra is summarized in Section 3.

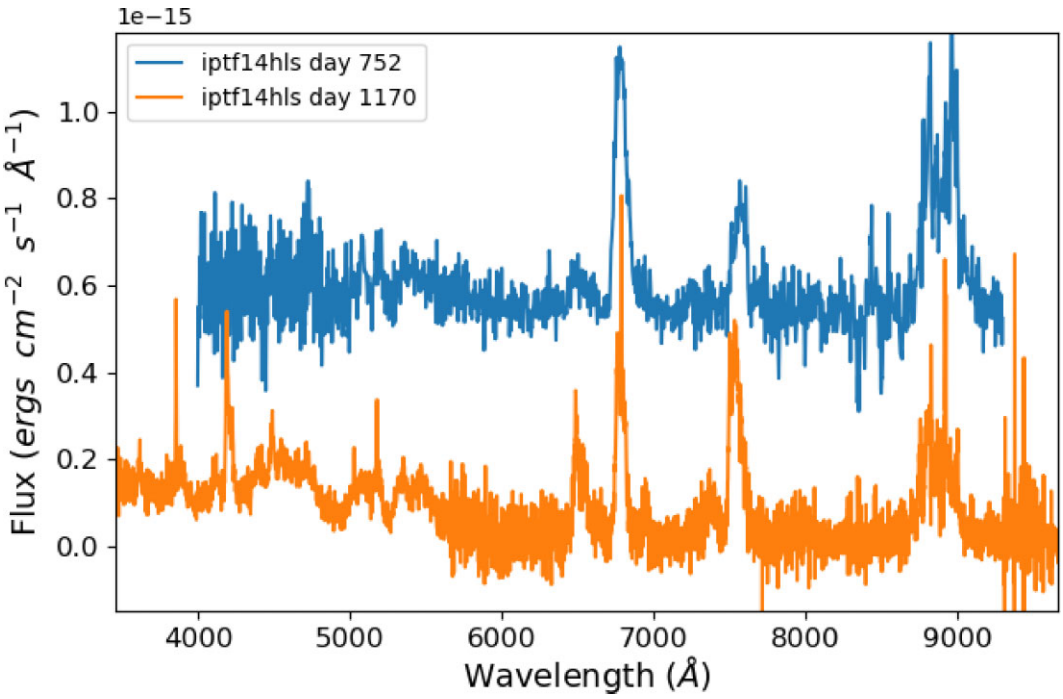

Figure A2. The evolution of the optical spectrum of iPTF14hls. Information on the spectra is summarized in Section 3.

This paper has been typeset from a TEX/LATEX file prepared by the author.